Geophysical Research Letters

RESEARCH LETTER
10.1029/2019GL086599

A Multi-Instrument Approach to Determining the Source-Region Extent of EEP-Driving EMIC Waves

A. T. Hendry[1], O. Santolik[1,2], Y. Miyoshi[3], A. Matsuoka[4], C. J. Rodger[5], M. A. Clilverd[6], C. A. Kletzing[7], M. Shoji[3], and I. Shinohara[4]

[1]Department of Space Physics, Institute of Atmospheric Physics, Czech Academy of Sciences, Prague, Czechia, [2]Faculty of Mathematics and Physics, Charles University, Prague, Czechia, [3]Institute for Space-Earth Environmental Research, Nagoya University, Nagoya, Japan, [4]Institute of Space and Astronautical Science, Japan Aerospace Exploration Agency, Sagamihara, Japan, [5]Department of Physics, University of Otago, Dunedin, New Zealand, [6]British Antarctic Survey (NERC), Cambridge, UK, [7]Department of Physics and Astronomy, University of Iowa, Iowa City, IA, USA

Key Points:

- The extent of an EEP-driving EMIC source region is estimated using conjunctions between in situ and ground-based observations
- A single EMIC wave event is observed simultaneously by conjugate RBSP-B and Arase spacecraft and ground-based instruments
- Conjugate measurements by the AARDDVARK network are used to track the EEP from the event and estimate the extent and drift rate

Correspondence to:
A. T. Hendry,
ath@ufa.cas.cz

Citation:
Hendry, A. T., Santolik, O., Miyoshi, Y., Matsuoka, A., Rodger, C. J., Clilverd, M. A., et al. (2020). A multi-instrument approach to determining the source-region extent of EEP-driving EMIC waves. *Geophysical Research Letters*, *47*, e2019GL086599. https://doi.org/10.1029/2019GL086599

Received 8 DEC 2019
Accepted 3 MAR 2020
Accepted article online 5 MAR 2020

Abstract Recent years have seen debate regarding the ability of electromagnetic ion cyclotron (EMIC) waves to drive EEP (energetic electron precipitation) into the Earth's atmosphere. Questions still remain regarding the energies and rates at which these waves are able to interact with electrons. Many studies have attempted to characterize these interactions using simulations; however, these are limited by a lack of precise information regarding the spatial scale size of EMIC activity regions. In this study we examine a fortuitous simultaneous observation of EMIC wave activity by the RBSP-B and Arase satellites in conjunction with ground-based observations of EEP by a subionospheric VLF network. We describe a simple method for determining the longitudinal extent of the EMIC source region based on these observations, calculating a width of 0.75 hr MLT and a drift rate of 0.67 MLT/hr. We describe how this may be applied to other similar EMIC wave events.

Plain Language Summary The Earth is surrounded by the Van Allen radiation belts, rings of high-energy charged particles trapped by the Earth's magnetic field. These particle populations are constantly changing, driven by forces from the Sun, Earth, and from the belts themselves. One of the most important drivers of this dynamism is the interaction between particles and electromagnetic waves. One such wave species, known as Electromagnetic Ion Cyclotron (EMIC) waves, has come under scrutiny recently due to experimental results calling into question the theoretical energy limits of their interactions with radiation belt electrons. Studying these waves and their interactions is hampered by our inability to accurately determine the size of the source region of these waves. In this study, we investigate a single EMIC wave event observed simultaneously by two separate satellites and use a network of ground-based radio wave receivers to estimate the size of the EMIC region. We also explain how the method used in this study may be generalized to other EMIC wave events. This method will allow us to carry out statistical analysis of the size of EMIC wave regions in general, aiding future research into the impacts of these waves on the radiation belts.

1. Introduction

Electromagnetic ion cyclotron (EMIC) waves, Pc1-2 (0.1–5 Hz) pulsations in the Earth's magnetosphere, have long been known as drivers of relativistic electron scattering and loss within the Earth's radiation belts (e.g., Thorne & Kennel, 1971). Despite decades of study, however, many basic elements of the interactions between EMIC waves and radiation belt electrons remain unknown. Key among these are the precise details of the process driving the electron scattering and the energy range across which this scattering can occur.

For many years, quasi-linear diffusion theory was the preferred approach to studying EMIC-driven electron precipitation. Under this theory, electron scattering is expected to be restricted to energies above roughly 1–2 MeV, only reaching lower energies in extraordinary cases (Meredith et al., 2003). However, in recent years a growing number of experimental studies have shown evidence of EMIC waves driving energetic electron precipitation (EEP) at energies below 500 keV (e.g., Millan et al., 2007; Woodger et al., 2015;

Clilverd et al., 2015; Rodger et al., 2015), with one study even suggesting that this lower-energy EEP may be the dominant form of EMIC-driven electron precipitation (Hendry et al., 2017). These results are largely incompatible with quasi-linear theory, and other possible explanations have been suggested, including nonlinear theory (e.g., Omura & Zhao, 2012, 2013), nonresonant theory (e.g., Chen et al., 2016), and resonant scattering by low-amplitude waves (Denton et al., 2019), although none has emerged as the dominant theory to date.

This uncertainty regarding the fundamental characteristics of EMIC waves is in part simply due to a lack of observations. It was not until fairly recently that EMIC waves were able to be conclusively linked to electron precipitation (Miyoshi et al., 2008; Rodger et al., 2008), and even now, we are limited to a handful of satellites for in situ study of these waves. Such limited and sporadic coverage makes it difficult at times to properly characterize the waves associated with a given precipitation event. The use of ground-based instrumentation has proved useful for filling some of these gaps in coverage.

There have been a number of investigations into the size of EMIC source regions (e.g., Blum et al., 2017; Engebretson et al., 2008, 2015; Lee et al., 2013; Mann et al., 2014). However, these studies have tended to focus on either the *L*-shell extent of the wave regions, which is typically much easier to determine, or have provided only very rough estimates of the longitudinal extent. Part of the reason for this is because it is generally not feasible to determine the longitudinal extent of an EMIC source region from in situ measurements alone. The combination of moving observation platforms and a low density of satellites means that, generally speaking, the size simply cannot be accurately calculated. Ground-based EMIC wave measurements do not fare much better—ionospheric ducting makes it all but impossible to determine precisely the source location of EMIC observations from ground-based wave observations alone (Kim et al., 2010). This in turn makes it very difficult to determine how large the source region is. Without precise knowledge of typical source-region extents, simulations and studies of EMIC waves have to essentially guess how large the source region is, or simply ignore this aspect entirely. This can lead to significant uncertainties regarding the effect of EMIC waves on radiation belt particle populsations as a whole—larger source regions allow not only more of the radiation belts to interact with the waves in question, but also for longer interaction times.

In this paper, we discuss a technique using subionospheric VLF wave observations for determining the longitudinal extent of a subset of EMIC waves, namely, those that are able to scatter energetic electrons into the loss cone. While this limitation excludes a significant proportion of the total EMIC wave population, it has the potential to provide much needed data on the wave characteristics of these EEP-driving waves.

2. Instrumentation

In this study we utilize in situ magnetic field observations from two sources: the RBSP Electric and Magnetic Field Instrument Suite and Integrated Science (EMFISIS) triaxial fluxgate magnetometer (MAG) (Kletzing et al., 2013) and the Arase Magnetic Field Experiment (MGF), which is also a triaxial fluxgate magnetometer (Matsuoka et al., 2018). These instruments sample at 64 and 256 Hz, respectively, making them ideal for investigating EMIC activity. We complement these observations with data from the 100 Hz ground-based search-coil magnetometer (SCM) located in Eskdalemuir, Scotland (55.3° N, −3.2° E, $L =\sim 2.8$), run by the British Geological Survey (Beggan & Musur, 2018). The ESK magnetometer consists of two coils: one arranged north-south and the other east-west.

For ground-based observation of electron fluxes, we use data from the Antarctic-Arctic Radiation-belt Dynamic Deposition VLF Atmospheric Research Konsortia (AARDDVARK) network. AARDDVARK is a global network of very low frequency (VLF) radio receivers, used to monitor the height of the ionospheric *D* region through the monitoring of powerful man-made VLF radio signals. VLF waves may propagate for very long distances through the Earth-Ionosphere waveguide. Changes in the height of the *D* region, for instance due to EEP into the ionosphere, change the properties of this waveguide, resulting in changes in the characteristics (i.e., phase and amplitude) of the received wave. By monitoring and investigating these changes, it is possible to derive information about electron precipitation into the ionosphere. More information on the AARDDVARK network and the remote sensing of the ionosphere can be found in Clilverd et al. (2009), and the sources within.

3. Event Description

3.1. Wave Observations: In Situ

As shown in Figure 1a, on 25 August 2018 from 20:46–21:05 UT, the RBSP-B EMFISIS MAG instrument observed a burst of EMIC wave activity between roughly 0.4–1.2 Hz, in the helium wave band ($\Omega_{He^+} < \omega < \Omega_{H^+}$). This activity consisted of two distinct wave bursts from 20:46–20:49 UT and 20:50–21:05 UT, with the peak wave amplitudes of 5.5 and 12.7 nT, respectively. A lower-amplitude burst of wave power was also observed in the hydrogen band ($\Omega_{O^+} < \omega < \Omega_{He^+}$) from roughly 1.2–1.6 Hz at around 21:04 UT; however, this was comparatively much weaker than the helium band wave, peaking at roughly 1.8 nT. We see evidence of rising-tone subpacket structures (sometimes called *fine-structure elements*; e.g., Matsuda et al., 2018), particularly during the second wave burst. Over the duration of this wave observation, the RBSP-B satellite traversed roughly L = 3.9–4.3, calculated using the 2002 Tsyganenko (T02) model (Tsyganenko, 2002a, 2002b) magnetic field model, at 20.7–21.2 MLT. RBSP-B was located close to the magnetic equator at this time, at a magnetic latitude of roughly −7.2°.

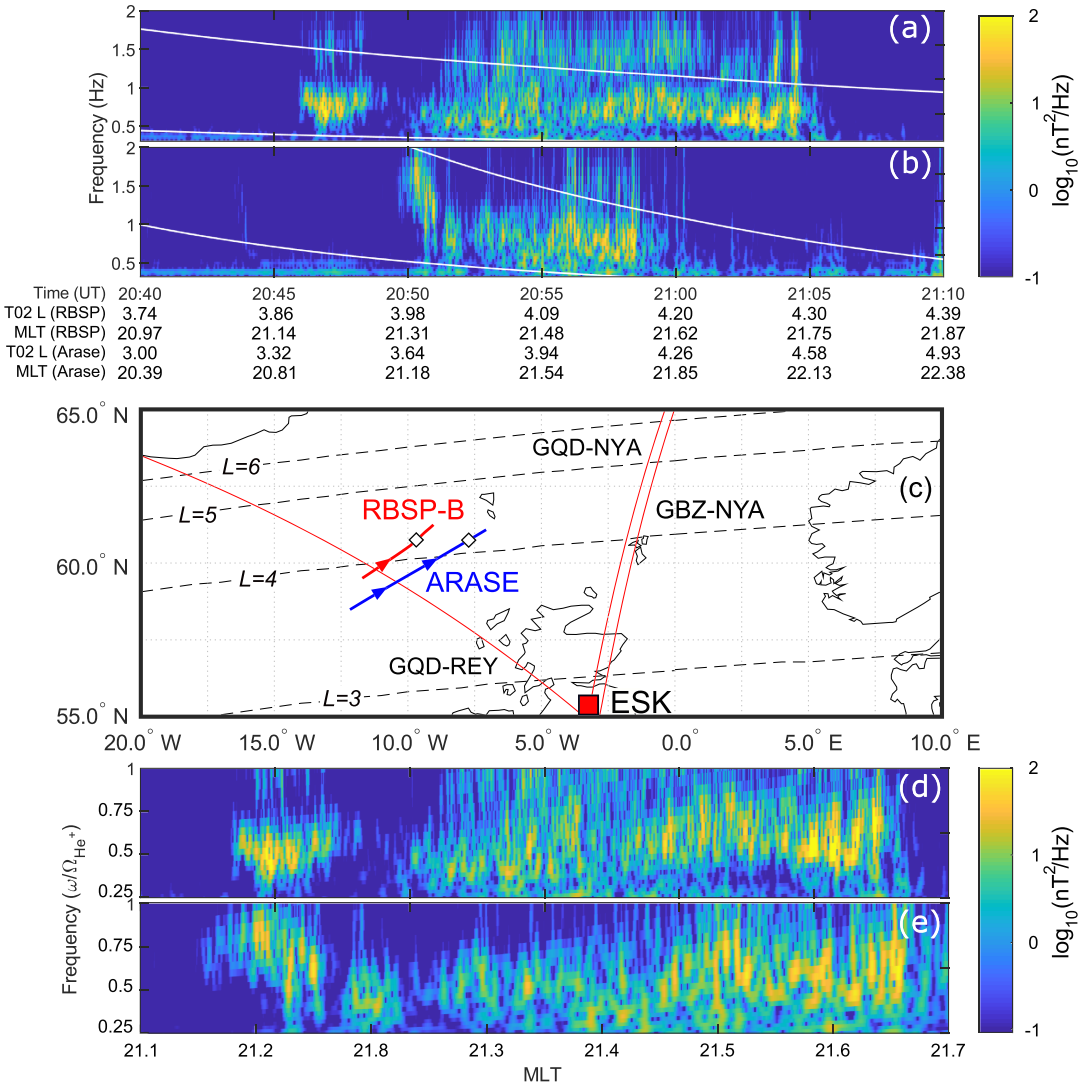

Figure 1. (a) Wavelet spectrogram of the RBSP-B perpendicular wave power (field-aligned coordinates), with the helium and oxygen gyrofrequencies plotted in white. (b) As in (a) but for the data from the Arase MGF instrument. (c) Map of the event region with the RBSP-B and Arase T02 footprints in red and blue, respectively (with arrows indicating the direction of travel and white diamonds indicating the point of closest approach); the 3 AARDDVARK VLF paths in red; and the Eskdalemuir SCM (red square). T02 L shells from 3–6 are shown as dashed black lines. (d and e) As in (a) and (b) but plotted against MLT and normalized by the equatorial helium gyrofrequency.

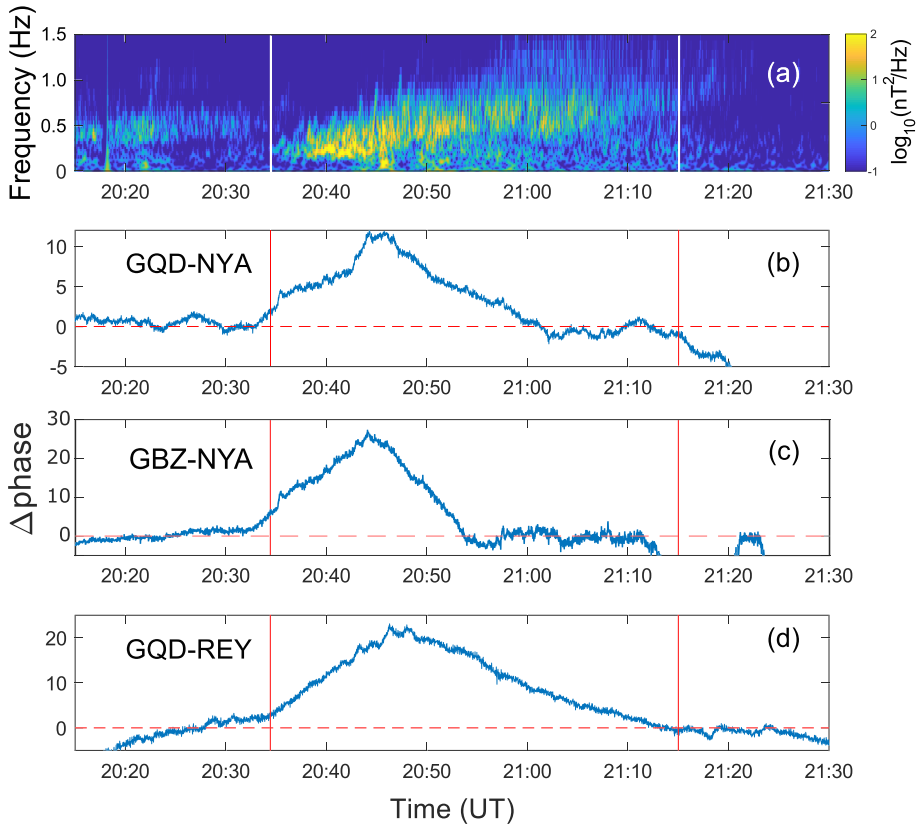

Figure 2. (a) Wavelet spectrogram of the ESK North-South component with the approximate temporal limits of the wave shown in white. (b) The difference between the phase of the GQD-NYA VLF signal at the event time and the QDC. (c) As in (b) for the GVT-NYA path. (d) As in (b) for the GQD-REY path. For panels (b)–(d), the dashed red lines indicate the zero point (i.e., the QDC), and the solid red lines indicate the temporal limits of the EMIC wave as seen at Eskdalemuir.

Figure 1a presents the wavelet spectrogram of the RBSP-B wave power perpendicular to the background field, calculated during the event period using the generalized Morse wavelet (Olhede & Walden, 2002) with symmetry parameter $\gamma = 3$. The equatorial helium and oxygen gyrofrequencies, Ω_{He^+} and Ω_{O^+}, respectively, are overplotted in white. The T02 footprint of the RBSP-B satellite during this period of wave observation, taken as the geographic coordinates of the magnetic field line traced down from the satellite to an altitude of 100 km, is shown in red in Figure 1c.

During this same time period, the Arase satellite was roughly in conjunction with RBSP-B. From roughly 20:49–20:59 UT, the Arase magnetometer observed strong wave power in the helium wave band. Like the RBSP-B observations, Arase saw two distinct wave bursts from 20:49–20:51 UT and 20:51–20:59 UT, peaking at 6.3 and 9.3 nT, respectively. During this wave observation, Arase traversed roughly $L = 3.6$–4.3 (T02) and 20.75–21.2 MLT. Arase was located much further down the field line than RBSP-B at a magnetic latitude of roughly −30°, likely outside the EMIC source region. The wavelet spectrogram of the Arase perpendicular wave power is presented in the same format as the RBSP-B data in Figure 1b. The T02 footprint of the Arase satellite during this period of wave observation is shown in blue in Figure 1c.

RBSP-B and Arase were not in perfect conjunction during this wave event, as is evident from examination of the footprint traces presented in Figure 1c—at every point during the wave event, the satellites were separated in either L shell or MLT. At closest approach, the satellites were separated by ~800 km when traced to the magnetic equator (using the T02 field model). Thus, a direct comparison between the wave observations is not necessarily the best approach to investigating the wave data. Figures 1d and 1e show the same data as Figures 1a and 1b, plotted against MLT instead of UT and with the frequency normalized by the equatorial helium gyrofrequency for each satellite. When viewed in this fashion, it is clear that these

observations are of the same wave event, with very strong similarities in the MLT locations of the wave observations.

3.2. Wave Observations: Ground Based

Evidence of EMIC wave activity was observed in the ESK SCM (Figure 1c, red square) at the same time as the satellite observations, shown in Figure 2a. This magnetometer is located roughly 5° southward and 5° eastward of the satellite footprint region—that is, roughly the same MLT and well within the limits of EMIC ducting (Kim et al., 2010). The wave seen in the ESK magnetometer was a clear IPDP-type (intervals of pulsations with diminishing periods) wave, with the average frequency of the wave gradually increasing over the observation period. We also see evidence of more rapid internal rising-tone subpacket structure. The wave activity on the ground lasts longer than the satellite observations, occurring for roughly 40 min from 20:35 UT until 21:15 UT, suggesting again that the satellites were passing through an existing wave source region, rather than observing the initial growth of the wave. In Figure 2a we have indicated the approximate temporal extent of the wave with vertical solid white lines, estimated as the times where the instantaneous sum of the wave power in the helium band returned to the background level.

3.3. EEP observations: Ground-based

There is growing experimental evidence to suggest that strong EMIC waves, particularly those with rising-tone subpacket structures, are capable of driving significant electron scattering into the loss cone, potentially through nonlinear interactions (e.g., Hendry et al., 2019; Kubota & Omura, 2017; Omura & Zhao, 2013). Thus, we expect that this wave event, which is both strong and features rising-tone subpacket structures, should drive electron precipitation into the upper atmosphere.

To get an idea of the electron precipitation being driven by this event, we can look at this event using ground-based instrumentation. The footprint region of this wave event is crossed by 10–15 AARDDVARK VLF paths, depending on the signals being observed at a given station. For this case study, a number of these were unusable due to poor signal strength or lack of phase lock. There is also overlap between some of the paths, providing essentially redundant data. We focus on the measurements from two AARDDVARK receivers located in Reykjavik, Iceland (REY), and Ny-Ålesund, Norway (NYA). For each of these receivers, we examine the signal from the British VLF transmitter located in Anthorn, UK (GQD). We also examine the signal from another British VLF transmitter in Skelton, UK (GVT), using data from the Ny-Ålesund, Norway (NYA), receiver. These paths are shown in Figure 1c; due to the scale of the map, the transmitter and receiver locations are not shown.

To examine the AARDDVARK data properly, we must estimate the *quiet-day curve* (QDC); that is, the form the signal would take in the absence of any atypical modification of the waveguide. For each of the paths studied, we construct an approximate QDC phase curve through a combination of detrending and analysis of quiet days prior to the event day. This QDC is then subtracted from the AARDDVARK signal, leaving only the changes to the signal caused by the EEP-driven ionization of the *D* region. For this study, we focus on the phase of the signal. The results of this are shown in Figures 2b, 2c, and 2d. The solid red lines indicate the period of wave activity, as determined by the ESK magnetometer.

The timing of this event is such that the terminator crosses each of the VLF paths during the event period. VLF phase and amplitude propagation are significantly complicated by the presence of the terminator, which can make detailed analysis of the VLF signal difficult. Fortunately, for our purposes, we take a less quantitative approach to this analysis, so precise knowledge of the phase and amplitude changes are not necessary.

In Figures 2b, 2c, and 2d, it is clear that there is EEP occurring along each of the paths, with significant changes in the measured phase of the signal in each case. We note that there are significant differences in the timing and duration of these phase changes; in the next section, we will investigate these changes in more detail, using the different locations of the paths to estimate the longitudinal extent of the EMIC source region.

4. Source-Region Analysis

From a combination of our in situ and ground-based observations, we are able to investigate the size and westward drift rate of the EMIC source region for this event. First, we investigate what the wave observations tell us about the source region.

From our ground-based EMIC wave observations, we know that this EMIC wave event began at roughly 20:35 UT, lasting for 40 min until 21:15 UT. Both the RBSP-B and Arase observations, from 20:46–21:05 UT and 20:49–20:59 UT, respectively, occur entirely within this time period, meaning that the limits of these in situ wave observations must represent spatial limits to the region occupied by the wave, rather than temporal limits. In other words, the onset and disappearance of wave activity in the satellites are due to the satellites entering the source region, rather than the source region forming and decaying around the satellites.

Based on the analysis of the satellite traces in Figure 1c, it is clear that the if the onset of wave activity on the satellites cannot be explained by temporal changes in the source region, then it must be due to the satellites passing through the western-most edge of the wave region; thus, by examining the satellite locations at these times, we can determine the MLT (or longitude) location of the western edge of the slowly westward drifting source region. By similar reasoning, it is clear that the disappearance of wave activity on the satellites is due to them reaching the upper L-shell extent of the EEP and EMIC source region.

The solid red and blue lines in Figure 1c trace T02 footprint RBSP-B and Arase satellites for the periods when each sees EMIC wave activity, that is, 20:45–21:04 UT for RBSP-B and 20:49–20:59 UT for Arase. From the endpoints of the interval, we can define a rough upper limit on the L-shell extent of the event region at $L = 4.3$. From the limits of the Arase observations, we know that the wave region must extend down to at least $L = 3.6$; however, we cannot rule out the possibility of the wave region extending lower. Other studies have used observations from the Polar-orbiting Operational Environmental Satellites (POES) constellation to estimate the L-shell extent of EMIC waves (e.g., Engebretson et al., 2015); however, due to extensive proton contamination of the POES electron data, this is not possible for this case.

Using the RBSP-B and Arase data, we can also estimate the drift rate of the source region relative to the Earth, from the slight differences in the satellite footprint locations at the onset of wave activity in each. The RBSP-B satellite first detected wave activity at 20:45:41, at which point the (T02) footprint of the satellite was located at a longitude of −11.69°E (21.14 MLT). The Arase satellite detected wave activity slightly later in time, starting at 20:49:23, at which point the (T02) footprint was located at a longitude of −12.15°E (21.14 MLT). This suggests that the westward boundary of the source region had drifted 0.46° westward in longitude over a period of roughly 5 min, giving a westward drift rate relative to the Earth of roughly 6°/hr. We cannot determine the extent of the source region purely from this; to complete the picture, we turn to the ground-based observations from AARDDVARK.

Starting with the REY path, shown in Figure 2c, we compare the change in phase to the ESK spectrogram plotted in Figure 2a. We can see that the phase change starts and ends roughly in sync with the wave seen at ESK, with the peak of the change in phase coinciding roughly with the peak wave intensity seen in the magnetometer. This suggests that the REY path overlaps with the EMIC source region for the entirety of the event period and that electron precipitation was occurring for the entire event period.

We turn now to the two NYA paths, from the GQD and GVT transmitters. For each of these paths, we note a phase change that starts in sync with the onset of the wave power in the ESK magnetometer, suggesting that the paths start the event period within the source region. Unlike the REY path, however, the phase changes on both of these paths return to zero before the wave power does. This return to zero indicates that no more electron precipitation is occurring along with path, which we attribute to the westward drift of the eastern boundary of the EMIC and EEP source regions, resulting in the eastern-most edge of the source region passing over these paths. Importantly, there is a slight difference in the times at which each path returns to zero, with roughly 6 min separating the them. Using this time offset together with the distance between the two paths, we can calculate the drift rate of the source region, relative to the Earth. Over the L-shell region for which we see waves in the satellite data, these two paths are separated by roughly 0.4° longitude, suggesting a westward drift rate of roughly 4°/hr. We note that this is almost identical to that calculated from the satellite footprints.

To determine the extent of the source region, we first assume that the point in time at which the phase change in the AARDDVARK paths returns to zero occurs when the eastern-most edge of the source region is directly over the path. We then use the calculated drift rates to extrapolate back in time, allowing us to determine the location of the eastern-most edge of the source region at the time of wave onset in the satellite data—the difference in this eastern edge and the western edge calculated from the satellite data gives us the extent of the wave source region. The GQD-NYA path returns to zero roughly 8 min after wave onset

in the RBSP-B satellite—if we average our two drift estimates and assume a 5°/hr westward drift rate, this suggests that the source region drifts west by roughly 0.67° longitude in this time. The mean longitude of the GQD-NYA path over the *L*-shell range of the satellite observations is −1.4°E. Thus, at the time of wave onset in the RBSP satellite, the eastern-most edge of the source region was located at a longitude of roughly −0.75°E. This gives us a total source region longitudinal extent of approximately 11°.

At times it may be more useful to determine the source region extent in terms of MLT, rather than geographic longitude, although we note that the drift calculations are typically simpler using longitude due to the inherent time dependence of MLT. Redoing the above calculation in terms of MLT, we determine a source region extent of roughly 0.83 hr MLT and an approximately negligible MLT drift rate—in other words, the source region is in fact stationary in MLT.

5. Discussion and Conclusions

We have demonstrated a method for determining the approximate longitudinal extent and drift rate of an EMIC source region using a combination of in situ spacecraft and ground-based measurements and the AARDDVARK network. The general process for an arbitrary event is as follows:

1. Determine the presence and footprint location of EMIC waves using in situ magnetometer observations. In situ wave observations for this step are not strictly necessary; however, we note that due to the ability of waves to duct significant distances upon reaching the Earth's ionosphere, the ground-based observation of waves is not sufficient to determine the presence of EMIC waves across a given AARDDVARK path. It may be possible to use a proxy instead of direct wave measurements, for instance the precipitation trigger described in Carson et al. (2013), for this purpose.
2. Determine the temporal extent of the wave using ground-based magnetometers. This step is important to provide context for the AARDDVARK measurements, to ensure that timing of the observed VLF signal changes match with the timing of the wave.
3. Determine the drift rate of the source region by comparing the times at which the source region boundaries cross the AARDDVARK paths. In this study, we used the time at which the phase change of the VLF signals (relative to the QDC calculated in section 3.3) returned to zero; however, the time of onset of phase changes is equally valid, provided that this onset is due to the source region drifting over the path.
4. Determine the eastern and western boundaries of the event by extrapolating from the path crossing times using the calculated drift rate. In this study, we were able to use the satellite data to determine the western edge of the source region; however, this may not always be possible. In theory this step can be performed with only two AARDDVARK paths (a minimum of two are required to calculate the drift speed relative to the Earth); however, in general, more paths will allow for a more accurate determination of the source-region size. From these measurements, calculating the size of the source region is fairly trivial, as we have shown.

We note that the above method will not be possible in all cases, as AARDDVARK coverage will not always be sufficient to calculate the require parameters.

We can draw comparisons between our method and that of Sakaguchi et al. (2015), who investigated the spatial scale size of EMIC-associated isolated proton aurora (IPA). The authors showed that individual IPA patches were typically less than 12° longitude wide, which places our event at the upper limit of this scale. However, we note that the size reported by Sakaguchi et al., 2015 is the size of individual IPA patches rather than the EMIC regions themselves, which may contain several distinct IPA patches.

A study by Zhang et al. (2016) used in situ and ground-based wave measurements to estimate the source region extent of a single EMIC wave event, estimating an extent of 2 hr for the H^+ band and 4 hr for the He^+ band. These are significantly larger than our own estimates; however, it must be noted that the use of ground-based wave measurements for determining source region extent is unreliable, due to the ducting issues mentioned previously. This could lead to a significant overestimation of the source region size. We also note that the Zhang et al. (2016) event occurred on the dayside, whereas our own event was well into the duskside—we cannot rule out an MLT dependence of the source region extent. Clearly, further study is required to determine if this is the case.

The use of the AARDDVARK network for determining the spatial extent of EMIC wave source regions has benefits over alternative methods. One of the greatest benefits is that of coverage. The AARDDVARK

network has the ability to remotely sense changes to the ionosphere in regions impossible for other ground-based instruments to be installed, including oceanic regions and the majority of the Southern Hemisphere. We note, however, that this range is a double-edged sword; care must be taken to ensure that precipitation observed by the AARDDVARK network is indeed due to the EMIC wave in question, and not due to some other precipitation source occurring elsewhere along the same VLF path. Care must also be taken to ensure a valid QDC is used to remove diurnal and other background variations in the signal—in this paper we used a simple method manually comparing the active period to quiet periods on surrounding days, a well-established method in the literature (e.g., Clilverd et al., 2006); however, we note that attempts have been made to automate this process (e.g., Neal et al., 2015).

In theory, a similar method should be possible with riometers; however, these are limited by their sensitivity and scope. Riometers are most sensitive to electron precipitation with energies of hundreds of keV and do not response strongly to relativistic electron precipitation. They can also only detect electron precipitation that occurs directly overhead the instrument, which limits their utility in such a study. With a dense enough riometer network, however, for instance the Canadian GO-RIO network, similar results should be possible.

The presented method is based on the assumption that the extent of the EMIC source region is the same as the extent of the EEP region. To justify this, we need only look to the AARDDVARK data presented earlier in this paper. In Figure 2d, we showed that the onset of the phase change in each of the paths lined up almost perfectly with the onset of EMIC wave power in the ESK magnetometer, suggesting that EMIC-driven electron scattering begins almost immediately after wave generation. This is supported by the literature as well; Omura and Zhao (2013) and Kubota and Omura (2017) both showed that electron precipitation occurs within seconds of interaction with rising-tone EMIC waves, such as the wave in this case study. We also note that the REY path, shown in Figure 2d, passes very close to the western edge of the event region, as defined by the RBSP-B and Arase satellites. This suggests that any longitudinal lag between the wave region and the precipitation region is likely very small.

Being able to determine the extent of EMIC source regions has important implications for the study of EMIC waves. When investigating the impact that EMIC waves have on radiation belt electron and ion populations, knowledge of the longitudinal extent of the EMIC wave region is essential—clearly, larger regions will have a greater effect on radiation belt populations. Being able to quantify this size will allow for more accurate simulations of EMIC wave-particle interactions, leading to better understanding of the scattering processes involved. Knowledge of the boundaries of the wave source region is also important for investigating EMIC wave generation, for instance determining how the scale of these regions varies across different wave observations, and whether this variation ties into other wave properties.

The clear downside of this technique is that it only works on EMIC waves that are actually capable of scattering electrons into the loss cone. In their study of EMIC-driven electron precipitation, Hendry et al. (2016) showed that there was a distinct difference between the spatial distribution of EEP-producing EMIC waves and EMIC waves as a whole, with EEP-producing EMIC waves typically occurring around magnetic midnight, well away from the typical peak in EMIC occurrence (e.g., Saikin et al., 2015). Thus, while this technique provides an invaluable insight into these EEP-producing waves, we must devise other techniques for determining the extent of other active EMIC waves.

There is an interesting aspect of the EMIC source region examined in this study that bears further investigation. One of the prevailing theories of IPDP-type wave generation suggests that the wave growth is driven by substorm-related ion injections at magnetic midnight, which drift clockwise (i.e., in a negative MLT direction) around the Earth (e.g., Yahnin et al., 2009). However, in section 4, we observed that the source region was in fact static with respect to MLT. This suggests that for this particular case study, ion injections are not the driving process of the wave generation. This is not without precedent; other studies of EMIC waves have seen source regions that do not drift in MLT (e.g., Hendry et al., 2016). At present, it is unclear what the true driving process might be; we hope to answer this in a future study.

As a proof of concept, this study shows that it is not only feasible, but is a relatively simple process to calculate the extent of an EEP-driving EMIC source region from the EEP signature in ground-based VLF measurements. We hope to expand this method into a broader study of EEP-driving EMIC waves, to derive statistics on the size of these wave regions. We hope that this will lead to a better understanding of the generation of EEP-driving EMIC waves, as well as the wave-particle interaction processes themselves.

Acknowledgments
The authors would like to thank the personnel who developed, maintain, and operate each of the satellites and instruments used in this study. Processing and analysis of EMFISIS data was performed under the support of JHU/APL Contract 921647 under NASA Prime Contract NAS5-01072 (EMFISIS data may be obtained from http://emfisis.physics.uiowa.edu/data/index). The search-coil magnetometer data used in this study are available from BGS on request. Science data of the ERG (Arase) satellite used in this study were obtained from the ERG Science Center operated by ISAS/JAXA and ISEE/Nagoya University (https://ergsc.isee.nagoya-u.ac.jp/index.shtml.en) (Miyoshi et al., 2018). The present study analyzed the MGF v01.00 data. AARDDVARK data availability is described at http://www.physics.otago.ac.nz/space/AARDDVARK_homepage.htm. This work has been supported by the postdoctoral program of the Czech Academy of Sciences and by its Praemium Academiae award and JSPS-19-05 project. A.T.H. and O.S. acknowledge funding received from the European Union's Horizon 2020 research and innovation programme under grant agreement No. 870452 (PAGER). O. S. also acknowledges support from Grants LTAUSA17070 and GACR18-05285S. This study is supported by Grants-in-Aid for Scientific Research (15H05815, 16H06286, and 17H00728) of Japan Society for the Promotion of Science (JSPS). This study was supported by JSPS Bilateral Open Partnership Joint Research Projects.

References

Beggan, C. D., & Musur, M. (2018). Observation of ionospheric Alfvén resonances at 1-30 hz and their superposition with the Schumann resonances. *Journal of Geophysical Research: Space Physics*, *123*, 4202–4214. https://doi.org/10.1029/2018JA025264

Blum, L. W., Bonnell, J. W., Agapitov, O., Paulson, K., & Kletzing, C. (2017). Emic wave scale size in the inner magnetosphere: Observations from the dual Van Allen Probes. *Geophysical Research Letters*, *44*, 1227–1233. https://doi.org/10.1002/2016GL072316

Carson, B. R., Rodger, C. J., & Clilverd, M. A. (2013). POES satellite observations of EMIC-wave driven relativistic electron precipitation during 1998–2010. *Journal of Geophysical Research: Space Physics*, *118*, 232–243. https://doi.org/10.1029/2012JA017998

Chen, L., Thorne, R. M., Bortnik, J., & Zhang, X.-J. (2016). Nonresonant interactions of electromagnetic ion cyclotron waves with relativistic electrons. *Journal of Geophysical Research: Space Physics*, *121*, 9913–9925. https://doi.org/10.1002/2016JA022813

Clilverd, M. A., Duthie, R., Hardman, R., Hendry, A. T., Rodger, C. J., Raita, T., et al. (2015). Electron precipitation from EMIC waves: A case study from 31 May 2013. *Journal of Geophysical Research: Space Physics*, *120*, 3618–3631. https://doi.org/10.1002/2015JA021090

Clilverd, M. A., Rodger, C. J., Thomson, N. R., Brundell, J. B., Ulich, T., Lichtenberger, J., et al. (2009). Remote sensing space weather events: Antarctic-Arctic Radiation-belt (Dynamic) Deposition-VLF Atmospheric Research Konsortium network. *Space Weather*, *7*(4). https://doi.org/10.1029/2008SW000412

Clilverd, M. A., Seppälä, A., Rodger, C. J., Verronen, P. T., & Thomson, N. R. (2006). Ionospheric evidence of thermosphere-to-stratosphere descent of polar nox. *Geophysical Research Letters*, *33*, L19811. https://doi.org/10.1029/2006GL026727

Denton, R. E., Ofman, L., Shprits, Y. Y., Bortnik, J., Millan, R. M., Rodger, C. J., et al. (2019). Pitch angle scattering of sub-MeV relativistic electrons by electromagnetic ion cyclotron waves. *Journal of Geophysical Research: Space Physics*, *124*, 5610–5626. https://doi.org/10.1029/2018JA026384

Engebretson, M. J., Lessard, M. R., Bortnik, J., Green, J. C., Horne, R. B., Detrick, D. L., et al. (2008). Pc1-Pc2 waves and energetic particle precipitation during and after magnetic storms: Superposed epoch analysis and case studies. *Journal of Geophysical Research: Space Physics*, *113*, A01211. https://doi.org/10.1029/2007JA012362

Engebretson, M. J., Posch, J. L., Wygant, J. R., Kletzing, C. A., Lessard, M. R., Huang, C.-L., et al. (2015). Van Allen probes, NOAA, GOES, and ground observations of an intense EMIC wave event extending over 12 h in magnetic local time. *Journal of Geophysical Research: Space Physics*, *120*, 5465–5488. https://doi.org/10.1002/2015JA021227

Hendry, A. T., Rodger, C. J., & Clilverd, M. A. (2017). Evidence of sub-MeV EMIC-driven electron precipitation. *Geophysical Research Letters*, *44*, 1210–1218. https://doi.org/10.1002/2016GL071807

Hendry, A. T., Rodger, C. J., Clilverd, M. A., Engebretson, M. J., Mann, I. R., Lessard, M. R., et al. (2016). Confirmation of EMIC wave driven relativistic electron precipitation. *Journal of Geophysical Research: Space Physics*, *121*, 5366–5383. https://doi.org/10.1002/2015JA022224

Hendry, A. T., Santolik, O., Kletzing, C. A., Rodger, C. J., Shiokawa, K., & Baishev, D. (2019). Multi-instrument observation of nonlinear emic-driven electron precipitation at sub-MeV energies. *Geophysical Research Letters*, *46*, 7248–7257. https://doi.org/10.1029/2019GL082401

Kim, H., Lessard, M. R., Engebretson, M. J., & Lühr, H. (2010). Ducting characteristics of Pc 1 waves at high latitudes on the ground and in space. *Journal of Geophysical Research*, *115*, A09310. https://doi.org/10.1029/2010JA015323

Kletzing, C. A., Kurth, W. S., Acuna, M., MacDowall, R. J., Torbert, R. B., Averkamp, T., et al. (2013). The electric and magnetic field instrument suite and integrated science (EMFISIS) on RBSP. *Space Science Reviews*, *179*(1), 127–181. https://doi.org/10.1007/s11214-013-9993-6

Kubota, Y., & Omura, Y. (2017). Rapid precipitation of radiation belt electrons induced by EMIC rising tone emissions localized in longitude inside and outside the plasmapause. *Journal of Geophysical Research: Space Physics*, *122*, 293–309. https://doi.org/10.1002/2016JA023267

Lee, J., Min, K., & Kim, K. (2013). Characteristic dimension of electromagnetic ion cyclotron wave activity in the magnetosphere. *Journal of Geophysical Research: Space Physics*, *118*, 1651–1658. https://doi.org/10.1002/jgra.50242

Mann, I. R., Usanova, M. E., Murphy, K., Robertson, M. T., Milling, D. K., Kale, A., et al. (2014). Spatial localization and ducting of EMIC waves: Van Allen Probes and ground-based observations. *Geophysical Research Letters*, *41*, 785–792. https://doi.org/10.1002/2013GL058581

Matsuda, S., Kasahara, Y., Miyoshi, Y., Nomura, R., Shoji, M., Matsuoka, A., et al. (2018). Spatial distribution of fine-structured and unstructured EMIC waves observed by the Arase satellite. *Geophysical Research Letters*, *45*, 11,530–11,538. https://doi.org/10.1029/2018GL080109

Matsuoka, A., Teramoto, M., Nomura, R., Nosé, M., Fujimoto, A., Tanaka, Y., et al. (2018). The Arase (ERG) magnetic field investigation. *Earth, Planets and Space*, *70*(1), 43.

Meredith, N. P., Thorne, R. M., Horne, R. B., Summers, D., Fraser, B. J., & Anderson, R. R. (2003). Statistical analysis of relativistic electron energies for cyclotron resonance with EMIC waves observed on CRRES. *Journal of Geophysical Research: Space Physics*, *108*, 1250. https://doi.org/10.1029/2002JA009700

Millan, R. M., Lin, R. P., Smith, D. M., & McCarthy, M. P. (2007). Observation of relativistic electron precipitation during a rapid decrease of trapped relativistic electron flux. *Geophysical Research Letters*, *34*, L10101. https://doi.org/10.1029/2006GL028653

Miyoshi, Y., Hori, T., Shoji, M., Teramoto, M., Chang, T.-F., Segawa, T., et al. (2018). The ERG science center. *Earth, Planets and Space*, *70*(1), 1–11.

Miyoshi, Y., Sakaguchi, K., Shiokawa, K., Evans, D., Albert, J., Connors, M., & Jordanova, V. (2008). Precipitation of radiation belt electrons by EMIC waves, observed from ground and space. *Geophysical Research Letters*, *35*, L23101. https://doi.org/10.1029/2008GL035727

Neal, J. J., Rodger, C. J., Clilverd, M. A., Thomson, N. R., Raita, T., & Ulich, T. (2015). Long-term determination of energetic electron precipitation into the atmosphere from AARDDVARK subionospheric VLF observations. *Journal of Geophysical Research: Space Physics*, *120*, 2194–2211. https://doi.org/10.1002/2014JA020689

Olhede, S. C., & Walden, A. T. (2002). Generalized morse wavelets. *IEEE Transactions on Signal Processing*, *50*(11), 2661–2670.

Omura, Y., & Zhao, Q. (2012). Nonlinear pitch angle scattering of relativistic electrons by EMIC waves in the inner magnetosphere. *Journal of Geophysical Research*, *117*, A08227. https://doi.org/10.1029/2012JA017943

Omura, Y., & Zhao, Q. (2013). Relativistic electron microbursts due to nonlinear pitch angle scattering by EMIC triggered emissions. *Journal of Geophysical Research: Space Physics*, *118*, 5008–5020. https://doi.org/10.1002/jgra.50477

Rodger, C. J., Hendry, A. T., Clilverd, M. A., Kletzing, C. A., Brundell, J. B., & Reeves, G. D. (2015). High-resolution in-situ observations of electron precipitation-causing EMIC waves. *Geophysical Research Letters*, *42*, 9633–9641. https://doi.org/10.1002/2015GL066581

Rodger, C. J., Raita, T., Clilverd, M. A., Seppälä, A., Dietrich, S., Thomson, N. R., & Ulich, T. (2008). Observations of relativistic electron precipitation from the radiation belts driven by EMIC waves. *Geophysical Research Letters*, *35*, L16106. https://doi.org/10.1029/2008GL034804

Saikin, A. A., Zhang, J. C., Allen, R. C., Smith, C. W., Kistler, L. M., Spence, H. E., et al. (2015). The occurrence and wave properties of H+-, He+-, and O+-band EMIC waves observed by the Van Allen Probes. *Journal of Geophysical Research: Space Physics*, *120*(9), 7477–7492.

Sakaguchi, K., Shiokawa, K., Miyoshi, Y., & Connors, M. (2015). Isolated proton auroras and Pc1/EMIC waves at subauroral latitudes. In Y. Zhang & L. J. Paxton (Eds.), *Auroral dynamics and space weather* (pp. 59–70): American Geophysical Union (AGU).

Thorne, R. M., & Kennel, C. F. (1971). Relativistic electron precipitation during magnetic storm main phase. *Journal of Geophysical research*, *76*(19), 4446–4453.

Tsyganenko, N. A. (2002a). A model of the near magnetosphere with a dawn-dusk asymmetry 1. Mathematical structure. *Journal of Geophysical Research*, *107*(A8), 1179. https://doi.org/10.1029/2001JA000219

Tsyganenko, N. A. (2002b). A model of the near magnetosphere with a dawn-dusk asymmetry 2. Parameterization and fitting to observations. *Journal of Geophysical Research*, *107*(A8), 1176. https://doi.org/10.1029/2001JA000220

Woodger, L. A., Halford, A. J., Millan, R. M., McCarthy, M. P., Smith, D. M., Bowers, G. S., et al. (2015). A summary of the BARREL campaigns: Technique for studying electron precipitation. *Journal of Geophysical Research: Space Physics*, *120*, 4922–4935. https://doi.org/10.1002/2014JA020874

Yahnin, A. G., Yahnina, T. A., Frey, H. U., Bösinger, T., & Manninen, J. (2009). Proton aurora related to intervals of pulsations of diminishing periods. *Journal of Geophysical Research*, *114*, A12215. https://doi.org/10.1029/2009JA014670

Zhang, X.-J., Li, W., Ma, Q., Thorne, R. M., Angelopoulos, V., Bortnik, J., et al. (2016). Direct evidence for EMIC wave scattering of relativistic electrons in space. *Journal of Geophysical Research: Space Physics*, *121*, 6620–6631. https://doi.org/10.1002/2016JA022521